www.sciencemag.org/cgi/content/full/science.aap8612/DC1

Supplementary Materials for

Rapid sea level rise in the aftermath of a Neoproterozoic snowball Earth

P. M. Myrow,* M. P. Lamb, R. C. Ewing

*Corresponding author. Email: pmyrow@coloradocollege.edu

Published 19 April 2018 on *Science* First Release
DOI: 10.1126/science.aap8612

This PDF file includes:

Materials and Methods

Particle Size

Point counts of thin sections (n=300) of the rhythmite lamination, which make up the preserved bedforms, indicate that the finer laminae contain 23% hematitic clay matrix, whereas the finer layers contain 34% matrix. These numbers include pseudomatrix that resulted from the breakdown of labile grains, so the original clay component is somewhat lower. Average grain sizes (n=50 each) of the framework grains of fine layers, after the data was transformed from thin section (2D) to equivalence in sieve data (*30*), is 0.037 mm (lower coarse silt) (standard deviation = 0.02), and 0.061 mm for the coarser layers (uppermost coarse silt) (standard deviation = 0.014).

Ripple Dimensions and Orientations

Several hierarchies of bedforms are preserved (Fig. 1a). First-order (i.e., the largest class) bedforms are straight-crested, relatively symmetrical ripples with heights of h=1.8±0.6cm (1σ), and crest-to-crest spacings of λ=33±11cm (Table S1). Their ripple aspect ratios (h/λ, where λ is ripple spacing and h is height) average 0.062 ± 0.02. The ripple symmetry index (RSI), which is the ratio of the width of the stoss to lee sides, averages 1.3 (range 1.1–1.7) (Table S2). Bedforms with RSI < 1.5 are considered to be symmetrical, and thus the first-order bedforms range from symmetrical to slightly asymmetrical. The second-order bedforms consist of symmetrical to moderately asymmetrical 2D ripples with h=0.4±0.2cm and λ=6.0±2.1cm (Table S1). Second order bedforms show locally developed bifurcations and minor additional defects typical of straight-crested wave ripples. The average aspect ratio for these smaller ripples is h/λ =0.06 ± 0.02, and the average RSI is 1.9±1.6 (Table S2). Rare, third-order bedforms, characterized by ~1-2 mm heights and 5-6 cm spacings, are parallel-to-oblique to the second-order bedforms.

The small ripples are oriented NNE–SSW (Fig. S1; Table S3), orthogonal to the first-order tidally influenced ripples, and thus wave action that generated the second-order ripples was likely normal to the tidal currents and consistent with expected equatorial easterlies given the low-latitude position of the deposit and NW oriented wind fields inferred from eolian dunes (*17*).

Accumulation Rate

We calculate the duration of the 16 m thick section at the top of the Elatina using an accumulation rate derived from data provided by Williams' (*13*) for the Elatina rhythmites. Williams' (*13*) counted 1580 laminae-cycle thicknesses and directly measured the total thickness of the core (9.39 m). Williams' calculated ~60 years for the accumulation of the 9.39 m core using thousands of measured sequential laminae thicknesses in a Fourier transform analysis. The power spectral density plots showed a frequency at 13.1 +/-0.1, which Williams' interpreted as representing the number of synodic (lunar) months per year at the time of deposition. Based on the details of the

lamination, including the alternation of thick and thin laminae cycles throughout the core, he was able to show that two laminae cycles represent one lunar month. He then made a calculation of duration as follows: 790 (laminae cycle pairs)/13.1(mo/yr) = 60.3 yr. The error of 0.1 on the 13.1 mo/yr estimate yields an error on the 60.3-year duration of +/- 0.46 years, or < 1%.

The (uncompacted) accumulation rate for Williams' core is 15.7 cm/yr, and thus our 16 m thick (uncompacted) interval yields an estimate of ~101.9 years. For uppermost silt size particles, compaction values between those typical of sand and silt are ~40% (*19*). Using a value of 40% compaction, we estimate a decompacted thickness of 27 m, which we use to generate an estimate of actual rate of sediment accumulation of 26.5 cm/yr. Greater depths result in higher compaction values. This is a conservative estimate that uses minimum values for percent compaction and assumes no erosion or non-deposition of sediment at the lamina scale during deposition; any minor erosion at the scale of a single lamina would only increase the calculated accumulation rate.

Paleo-hydraulics

Ripple aspect ratios for orbital and anorbital ripples, whether formed on sandy or silty beds, collapse to the relation (*16*, *28*) (Fig. 3a)

$$\frac{h}{\lambda} = \exp\left(-0.095\left(\ln\frac{d_0}{h} \right)^2 + 0.442 \ln\frac{d_0}{h} - 2.28 \right) \qquad (1)$$

where h is ripple height, λ, is ripple spacing, and d_0 is wave near-bed orbital diameter. Inserting $h/\lambda = 0.06 \pm 0.02$ (one standard deviation) and $h = 0.004 \pm 0.002$ m into Eq (1) yields $d_0 = 0.95 \pm 0.15$ m. To estimate d_0 and wave period, T, as a function of water depth and wind speed, we first use the intermediate-wave model of (*31*, *32*) to find wave height and T assuming a fetch based on paleogeographic reconstructions (*10*) of 75 km. Next, similar to (*33*), we use Airy wave theory and an iterative scheme to find water depth and wind speed combinations that produce a given orbital diameter. The wind speeds reported are average wind speeds during ripple-forming events with averaging timescales of at least 3-5 hours (*31*). Varying the fetch within a factor of two (38 km – 150 km) shifts the water depth constraints by ~1 m. The reconstruction also yields estimates of wave height and wave orbital velocity (Fig. S2). If depth did not vary, then sea level must have risen to match sediment accumulation at 27 cm/yr. If depth shallowed to its maximum extent of 7 m during accumulation, as allowed by the variance in reconstructed d_0 from ripple dimensions, then the remaining 20 m of accumulation must have been accommodated by sea level rise at a rate of 20 cm/yr.

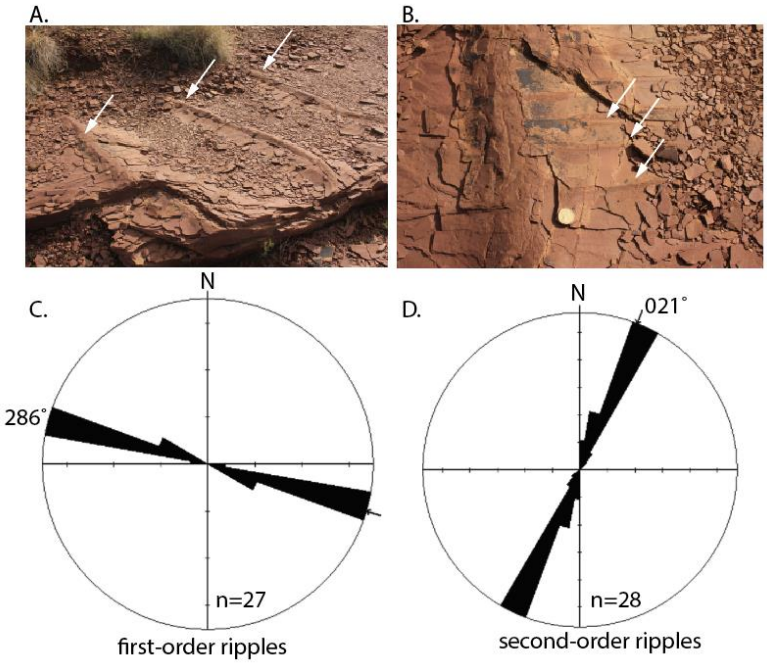

Fig. S1. Ripple Orientations. Measurements of first- and second-order ripples at Lat: S 32.41899, Long: E 137.72365 (Table S3). (A) First-order ripple crests highlighted by white arrows. (B) second order ripple crests highlighted by white arrows. Note second-order crests are perpendicular to first-order crest. (C) Rose diagram showing the orientation of first-order crests measured at this locality. (D) Rose diagram showing the ripple orientation of second-order crests measured at this locality. All measurements are rotated 30 ° east to represent Cryogenian paleonorth (c.f. 5, 9, 34).

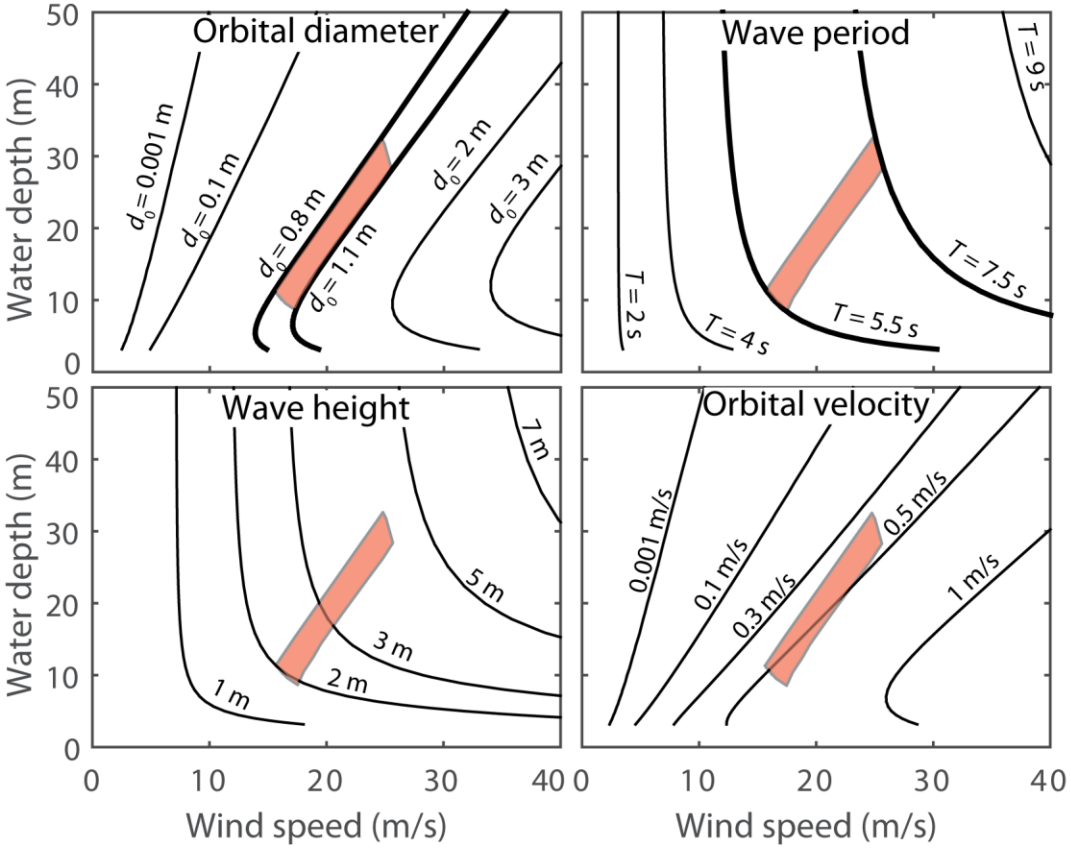

Fig. S2. Paleohydraulic reconstruction. Possible combinations of average wind speed and water depth that are capable of producing certain values of wave orbital diameter, significant wave period, significant wave height and near-bed orbital velocity according to Airy wave theory and a theory for generating intermediate-depth wind-driven waves (*31*, *32*). The orange shaded region represents the parameter space consistent with Elatina wave ripples, namely orbital diameters of $d_0 = 0.95 \pm 0.15$ m and wave periods, T, of 5.5 – 7.5 s. The wind speeds reported are average wind speeds during ripple-forming events with averaging timescales of at least 3–5 hours (*31*). For a given average wind speed during ripple forming wind events, water depth is predicted to have not changed by more than 7 m in order to produce ripples under waves with $d_0 = 0.95 \pm 0.15$ m. For wind speeds of ~16 m/s, consistent with the estimate of (*8*), the water depth is predicted to have been 9–16 m given the uncertainty in d_0. Larger changes in reconstructed water depth would require unlikely covariation between average wind speed, wave period, wave height and water depth to hold $d_0 = 0.95 \pm 0.15$. The paleohydraulic reconstruction is based on a 75 km fetch inferred from paleogeographic reconstructions (*10*); varying the fetch within a factor of two (38 km – 150 km) has a negligible effect on the water depth reconstruction.

Table S1. Ripple Dimensions.

Ripple order	Height (cm)	Crest-crest spacing (cm)	Ripple aspect
1	1.3	31	0.04
1	0.5	55	0.01
1	1.9	32	0.06
1	1.9	44	0.04
1	2.3	47	0.05
1	2.6	44	0.06
1	2.3	43.5	0.05
1	1.3	25.5	0.05
1	1.5	23	0.07
1	1.2	24	0.05
1	1.9	29	0.07
1	1.3	26	0.05
1	1.9	24	0.08
1	1.6	22	0.07
1	1.4	19	0.07
1	2.1	29	0.07
1	2.5	30	0.08
1	2.8	22	0.13
1	2.1	48	0.04
1	2.6	46	0.06
1	1	24	0.04
2	0.2	10	0.02
2	0.2	6	0.03
2	0.4	8	0.05
2	0.2	6	0.03
2	0.2	4	0.05
2	0.3	2.2	0.14
2	0.3	3.6	0.08
2	0.2	5.1	0.04
2	0.2	6.3	0.03
2	0.1	2.9	0.03
2	0.2	3.1	0.06
2	0.3	3.6	0.08
2	0.4	3.4	0.12
2	0.3	3.5	0.09
2	0.3	3	0.10
2	0.3	4.5	0.07
2	0.4	3	0.13
2	0.5	3.5	0.14
2	0.2	4	0.05

2	0.2	4	0.05
2	0.3	6	0.05
2	0.3	5	0.06
2	0.2	4.5	0.04
2	0.1	3.7	0.03
2	0.1	3.3	0.03
2	0.3	8	0.04
2	0.3	6	0.05
2	0.3	4.4	0.07
2	0.3	5.5	0.05
2	0.2	5	0.04
2	0.4	6	0.07
2	0.4	6.6	0.06
2	0.3	6.4	0.05
2	0.2	4.5	0.04
2	0.2	4.5	0.04
2	0.1	5	0.02
2	0.3	5	0.06
2	0.4	5.3	0.08
2	0.3	4.9	0.06
2	0.3	5.1	0.06
2	0.2	5.3	0.04
2	0.2	4.5	0.04
2	0.4	5.5	0.07
2	0.3	5.6	0.05
2	0.2	4.4	0.05
2	0.3	6	0.05
2	0.4	5	0.08
2	0.4	6.3	0.06
2	0.4	6.7	0.06
2	0.2	6	0.03
2	0.4	6.5	0.06
2	0.3	5.5	0.05
2	0.1	7.5	0.01
2	0.2	3	0.07
2	0.2	3.8	0.05
2	0.3	2.7	0.11
2	0.2	3.5	0.06
2	0.3	2	0.15
2	0.2	3.6	0.06
2	0.3	4	0.08
2	0.3	3.9	0.08
2	0.4	7	0.06
2	0.4	7	0.06

2	0.4	6.5	0.06
2	0.4	8	0.05
2	0.6	8	0.08
2	0.6	9.5	0.06
2	0.7	7.5	0.09
2	0.4	7.5	0.05
2	0.4	6.5	0.06
2	0.2	4.5	0.04
2	0.3	3.5	0.09
2	0.3	5.3	0.06
2	0.2	5.7	0.04
2	0.4	4.5	0.09
2	0.6	5.5	0.11
2	0.4	5.3	0.08
2	0.3	4.9	0.06
2	0.4	7.3	0.05
2	0.5	9	0.06
2	0.6	10.5	0.06
2	0.5	6	0.08
2	0.3	6.5	0.05
2	0.4	4.5	0.09
2	0.5	6	0.08
2	0.5	8.5	0.06
2	0.6	9.5	0.06
2	0.4	10.5	0.04
2	0.3	8.8	0.03
2	0.3	7.7	0.04
2	0.4	6.5	0.06
2	0.4	7	0.06
2	0.5	7.5	0.07
2	0.2	5	0.04
2	0.3	4.5	0.07
2	0.4	6.1	0.07
2	0.5	7.4	0.07
2	0.4	7	0.06
2	0.3	5.5	0.05
2	0.4	5.8	0.07
2	0.3	5.4	0.06
2	0.5	5.8	0.09
2	0.5	7.5	0.07
2	0.3	9	0.03
2	0.9	12	0.08
2	1	13	0.08
2	0.8	10.5	0.08
2	0.5	8.5	0.06

2	0.5	8	0.06
2	0.5	7	0.07
2	0.5	8	0.06
2	0.5	7.5	0.07
2	0.4	7.1	0.06
2	0.8	6.3	0.13
2	0.7	7.9	0.09
2	0.5	9.2	0.05

Table S2. Ripple Asymmetry.

Ripple Order	Crest-trough spacing (cm)	Trough-crest spacing (cm)	RAI
1	16	15	1.07
1	20	12	1.67
1	25	19	1.32
1	25	19	1.32
1	21.5	20	1.08
1	14	11.5	1.22
1	12.5	10.5	1.19
1	14	10	1.40
1	16.5	12.5	1.32
1	14	12	1.17
1	14	10	1.40
1	13	9	1.44
1	10	9	1.11
1	15	14	1.07
1	17.5	12.5	1.40
1	13.5	8.5	1.59
2	1	2.8	0.36
2	0.5	1	0.50
2	2.5	4.5	0.56
2	3	5	0.60
2	3	5	0.60
2	3.1	4.8	0.65
2	2.3	3.5	0.66
2	2	3	0.67
2	3	4.5	0.67
2	2	3	0.67
2	2.2	3.3	0.67
2	3.5	5	0.70
2	3.5	5	0.70
2	4	5.5	0.73
2	3	4.1	0.73
2	5.5	7.5	0.73
2	1.5	2	0.75
2	1.5	2	0.75
2	2.5	3.3	0.76
2	3.5	4.5	0.78
2	4	5	0.80
2	2.2	2.7	0.81
2	2.7	3.3	0.82

2	3.3	4	0.83
2	1	1.2	0.83
2	4	4.8	0.83
2	4.2	5	0.84
2	2.9	3.4	0.85
2	3	3.5	0.86
2	3	3.5	0.86
2	3.5	4	0.88
2	3.5	4	0.88
2	2.5	2.8	0.89
2	4.5	5	0.90
2	5	5.5	0.91
2	5	5.5	0.91
2	3.7	4	0.93
2	1.4	1.5	0.93
2	3	3.2	0.94
2	2.2	2.3	0.96
2	2.7	2.8	0.96
2	3	3.1	0.97
2	3	3	1.00
2	2	2	1.00
2	2	2	1.00
2	1.6	1.6	1.00
2	2	2	1.00
2	2.5	2.5	1.00
2	2.5	2.5	1.00
2	3	3	1.00
2	1	1	1.00
2	4	4	1.00
2	3	3	1.00
2	3.5	3.5	1.00
2	3.5	3.5	1.00
2	2.7	2.7	1.00
2	6	6	1.00
2	2.8	2.7	1.04
2	3.3	3	1.10
2	3.9	3.5	1.11
2	4.5	4	1.13
2	4	3.5	1.14
2	3.5	3	1.17
2	3.5	3	1.17
2	3.5	3	1.17
2	3	2.5	1.20
2	2.7	2.2	1.23

2	2	1.6	1.25
2	2.5	2	1.25
2	2.5	2	1.25
2	5	4	1.25
2	3	2.3	1.30
2	1.7	1.3	1.31
2	4	3	1.33
2	2.3	1.7	1.35
2	2.6	1.9	1.37
2	3.5	2.5	1.40
2	5	3.5	1.43
2	5	3.5	1.43
2	6	4	1.50
2	1.5	1	1.50
2	3	2	1.50
2	2.4	1.5	1.60
2	4	2.5	1.60
2	2.5	1.5	1.67
2	1.7	1	1.70
2	4	2.3	1.74
2	3.5	2	1.75
2	2.3	1.3	1.77
2	3.7	2	1.85
2	4	2	2.00
2	4	2	2.00
2	4	2	2.00
2	3	1.5	2.00
2	3	1.5	2.00
2	2.5	1.2	2.08
2	2.5	1.1	2.27
2	3.7	1.6	2.31
2	3.5	1.5	2.33
2	3.5	1.5	2.33
2	2.4	1	2.40
2	2.4	1	2.40
2	2.5	1	2.50
2	4	1.6	2.50
2	4.5	1.8	2.50
2	5	2	2.50
2	2.5	1	2.50
2	2.9	1.1	2.64
2	4	1.5	2.67
2	2.2	0.8	2.75
2	5.5	2	2.75
2	5	1.7	2.94

2	6	2	3.00
2	6	2	3.00
2	3	1	3.00
2	3.4	1.1	3.09
2	4.2	1.3	3.23
2	6.5	2	3.25
2	3.5	1	3.50
2	3.5	1	3.50
2	4.3	1.2	3.58
2	4.2	1.1	3.82
2	3.2	0.8	4.00
2	4.5	1	4.50
2	5.5	1.1	5.00
2	5	1	5.00
2	3.8	0.7	5.43
2	3	0.5	6.00
2	5.2	0.8	6.50
2	5.6	0.8	7.00
2	3.9	0.5	7.80
2	4.5	0.5	9.00
2	2.7	0.3	9.00

Table S3. Ripple Orientations. See Fig. S2 for details.

First-order ripples orientation (degrees)	**Second-order ripples** orientation (degrees)
283	3
296	5
293	13
292	23
288	33
283	41
293	34
273	26
287	28
285	25
283	23
288	23
283	23
283	25
286	25
286	25
283	23
283	23
288	23
293	22
298	21
288	18
288	18
278	3
283	13
288	16
283	16

References and Notes

1. H. D. Pritchard, S. R. M. Ligtenberg, H. A. Fricker, D. G. Vaughan, M. R. van den Broeke, L. Padman, Antarctic ice-sheet loss driven by basal melting of ice shelves. *Nature* **484**, 502–505 (2012). doi:10.1038/nature10968 Medline

2. P. F. Hoffman, D. S. Abbot, Y. Ashkenazy, D. I. Benn, J. J. Brocks, P. A. Cohen, G. M. Cox, J. R. Creveling, Y. Donnadieu, D. H. Erwin, I. J. Fairchild, D. Ferreira, J. C. Goodman, G. P. Halverson, M. F. Jansen, G. Le Hir, G. D. Love, F. A. Macdonald, A. C. Maloof, C. A. Partin, G. Ramstein, B. E. J. Rose, C. V. Rose, P. M. Sadler, E. Tziperman, A. Voigt, S. G. Warren, Snowball Earth climate dynamics and Cryogenian geology-geobiology. *Sci. Adv.* **3**, e1600983 (2017). doi:10.1126/sciadv.1600983 Medline

3. J. L. Kirschvink, "Late Proterozoic low-latitude glaciation: The snowball Earth," in *The Proterozoic Biosphere*, J. W. Schopf and C. Klein, Eds. (Cambridge Univ. Press, 1992); pp. 51–52.

4. J. Yang, M. F. Jansen, F. A. Macdonald, D. S. Abbot, Persistence of a freshwater surface ocean after a snowball Earth. *Geology* **45**, 615–618 (2017). doi:10.1130/G38920.1

5. P. F. Hoffman, A. J. Kaufman, G. P. Halverson, D. P. Schrag, A Neoproterozoic snowball earth. *Science* **281**, 1342–1346 (1998). doi:10.1126/science.281.5381.1342 Medline

6. R. I. F. Trindade, E. Font, M. S. D'Agrella-Filho, A. C. R. Nogueira, C. Riccomini, Low-latitude and multiple geomagnetic reversals in the Neoproterozoic Puga cap carbonate, Amazon craton. *Terra Nova* **15**, 441–446 (2003). doi:10.1046/j.1365-3121.2003.00510.x

7. B. Kilner, C. Mac Niocaill, M. Brasier, Low-latitude glaciation in the Neoproterozoic of Oman. *Geology* **33**, 413–416 (2005). doi:10.1130/G21227.1

8. C. V. Rose, A. C. Maloof, B. Schoene, R. C. Ewing, U. Linnemann, M. Hofmann, J. M. Cottle, The End-Cryogenian Glaciation of South Australia. *Geosci. Can.* **40**, 256–293 (2013). doi:10.12789/geocanj.2013.40.019

9. D. A. D. Evans, T. D. Raub, Neoproterozoic glacial palaeolatitudes: A global update. *Geol. Soc. London Memoirs* **36**, 93–112 (2011).

10. W. V. Preiss, "Stratigraphic nomenclature and classification," in *The Adelaide Geosyncline: Late Proterozoic Stratigraphy, Sedimentation, Palaeontology and Tectonics*, W. V. Preiss, Ed. (Bulletin 53, Geological Survey of South Australia, 1987), pp. 29–34.

11. Materials and methods are available as supplementary materials.

12. G. E. Williams, Sunspot periods in the late Precambrian glacial climate and solar–planetary relations. *Nature* **291**, 624–628 (1981). doi:10.1038/291624a0

13. G. E. Williams, Late Precambrian tidal rhythmites in South Australia and the history of the Earth's rotation. *J. Geol. Soc. London* **146**, 97–111 (1989). doi:10.1144/gsjgs.146.1.0097

14. P. M. Myrow, W. Fischer, J. W. Goodge, Wave-modified turbidites: Combined-flow shoreline and shelf deposits, Cambrian, Antarctica. *J. Sediment. Res.* **72**, 641–656 (2002). doi:10.1306/022102720641

15. H. E. Clifton, J. R. Dingler, "Wave-formed structures and paleoenvironmental reconstruction," in *Wave-Dominated Coastal Environments*, B. Greenwood, R. A. Davis, Jr., Eds. (Elsevier, 1984) pp. 165–198.

16. M. P. Lamb, J. D. Parsons, High-density suspensions formed under waves. *J. Sediment. Res.* **75**, 386–397 (2005). doi:10.2110/jsr.2005.030

17. G. E. Williams, Late Neoproterozoic periglacial aeolian sand sheet, Stuart Shelf, South Australia. *Aust. J. Earth Sci.* **45**, 733–741 (1998). doi:10.1080/08120099808728429

18. P. W. Schmidt, G. E. Williams, The Neoproterozoic climatic paradox: Equatorial palaeolatitude for Marinoan glaciation near sea level in South Australia. *Earth Planet. Sci. Lett.* **134**, 107–124 (1995). doi:10.1016/0012-821X(95)00106-M

19. J. P. Grotzinger, S. Gupta, M. C. Malin, D. M. Rubin, J. Schieber, K. Siebach, D. Y. Sumner, K. M. Stack, A. R. Vasavada, R. E. Arvidson, F. Calef 3rd, L. Edgar, W. F. Fischer, J. A. Grant, J. Griffes, L. C. Kah, M. P. Lamb, K. W. Lewis, N. Mangold, M. E. Minitti, M. Palucis, M. Rice, R. M. E. Williams, R. A. Yingst, D. Blake, D. Blaney, P. Conrad, J. Crisp, W. E. Dietrich, G. Dromart, K. S. Edgett, R. C. Ewing, R. Gellert, J. A. Hurowitz, G. Kocurek, P. Mahaffy, M. J. McBride, S. M. McLennan, M. Mischna, D. Ming, R. Milliken, H. Newsom, D. Oehler, T. J. Parker, D. Vaniman, R. C. Wiens, S. A. Wilson, Deposition, exhumation, and paleoclimate of an ancient lake deposit, Gale crater, Mars. *Science* **350**, aac7575 (2015). doi:10.1126/science.aac7575 Medline

20. C. A. Partin, P. M. Sadler, Slow net sediment accumulation sets snowball Earth apart from all younger glacial episodes. *Geology* **44**, 1019–1022 (2016). doi:10.1130/G38350.1

21. E. Carminati, G. Martinelli, Subsidence rates in the Po Plain, northern Italy: The relative impact of natural and anthropogenic causation. *Eng. Geol.* **66**, 241–255 (2002). doi:10.1016/S0013-7952(02)00031-5

22. P. F. Hoffman, Strange bedfellows: Glacial diamictite and cap carbonate from the Marinoan (635 Ma) glaciation in Namibia. *Sedimentology* **58**, 57–119 (2011). doi:10.1111/j.1365-3091.2010.01206.x

23. J. R. Creveling, J. X. Mitrovica, The sea-level fingerprint of a Snowball Earth deglaciation. *Earth Planet. Sci. Lett.* **399**, 74–85 (2014). doi:10.1016/j.epsl.2014.04.029

24. T. M. Cronin, Rapid sea-level rise. *Quat. Sci. Rev.* **56**, 11–30 (2012). doi:10.1016/j.quascirev.2012.08.021

25. T. Hanebuth, K. Stattegger, P. M. Grootes, Rapid flooding of the Sunda Shelf: A late-glacial sea-level record. *Science* **288**, 1033–1035 (2000). doi:10.1126/science.288.5468.1033 Medline

26. R. C. Ewing, I. Eisenman, M. P. Lamb, L. Poppick, A. C. Maloof, W. W. Fischer, New constraints on equatorial temperatures during a Late Neoproterozoic snowball Earth glaciation. *Earth Planet. Sci. Lett.* **406**, 110–122 (2014). doi:10.1016/j.epsl.2014.09.017

27. P. A. Allen, P. F. Hoffman, Extreme winds and waves in the aftermath of a Neoproterozoic glaciation. *Nature* **433**, 123–127 (2005). doi:10.1038/nature03176 Medline

28. P. L. Wiberg, C. K. Harris, Ripple geometry in wave-dominated environments. *J. Geophys. Res. Oceans* **99**, 775–789 (1994). doi:10.1029/93JC02726

29. Z. J. You, B. Yin, A unified criterion for initiation of sediment motion and inception of sheet flow under water waves. *Sedimentology* **53**, 1181–1190 (2006). doi:10.1111/j.1365-3091.2006.00810.x

30. M. R. Johnson, Thin section grain size analysis revisited. *Sedimentology* **41**, 985–999 (1994). doi:10.1111/j.1365-3091.1994.tb01436.x

31. Coastal Engineering Research Center, *Shore Protection Manual* (Department of the Army, Waterways Experiment Station, Corps of Engineers, 1984).

32. K. Hasselmann, W. Sell, D. B. Ross, P. Müller, A parametric wave prediction model. *J. Phys. Oceanogr.* **6**, 200–228 (1976). doi:10.1175/1520-0485(1976)006<0200:APWPM>2.0.CO;2

33. M. P. Lamb, W. Fischer, T. D. Raub, J. T. Perron, P. M. Myrow, Origin of giant wave ripples in snowball Earth cap carbonate. *Geology* **40**, 827–830 (2012). doi:10.1130/G33093.1

34. P. W. Schmidt, G. E. Williams, M. O. McWilliams, Palaeomagnetism and magnetic anisotropy of late Neoproterozoic strata, South Australia: Implications for the palaeolatitude of late Cryogenian glaciation, cap carbonate and the Ediacaran System. *Precambrian Res.* **174**, 35–52 (2009). doi:10.1016/j.precamres.2009.06.002